HHS Public Access

Author manuscript

J Control Release. Author manuscript; available in PMC 2018 January 10.

Published in final edited form as:

J Control Release. 2017 January 10; 245: 81–94. doi:10.1016/j.jconrel.2016.11.013.

Tumor-targeted delivery of sunitinib base enhances vaccine therapy for advanced melanoma by remodeling the tumor microenvironment

Meirong Huo[a,b], **Yan Zhao**[a,c], **Andrew Benson Satterlee**[a,d], **Yuhua Wang**[a], **Ying Xu**[a,e], and **Leaf Huang**[a,*]

[a]Division of Molecular Pharmaceutics, Center for Nanotechnology in Drug Delivery, Eshelman School of Pharmacy, University of North Carolina at Chapel Hill, Chapel Hill, North Carolina 27599, United States

[b]State Key Laboratory of Natural Medicines, Department of Pharmaceutics, China Pharmaceutical University, Nanjing 210009, China

[c]Department of Pharmaceutics, School of Pharmacy, China Medical University, Shenyang 110122, China

[d]UNC and NCSU Joint Department of Biomedical Engineering, Chapel Hill, NC 27599, United States

[e]Department of Pharmaceutics, School of Pharmacy, Jiangsu University, Zhenjiang 212013, China

Abstract

Development of an effective treatment against advanced tumors remains a major challenge for cancer immunotherapy. We have previously developed a potent mannose-modified lipid calcium phosphate (LCP) nanoparticle (NP)-based Trp2 vaccine for melanoma therapy, but because this vaccine can induce a potent anti-tumor immune response only during the early stages of melanoma, poor tumor growth inhibition has been observed in more advanced melanoma models, likely due to the development of an immune-suppressive tumor microenvironment (TME). To effectively treat this aggressive tumor, a multi-target receptor tyrosine kinase inhibitor, sunitinib base, was efficiently encapsulated into a targeted polymeric micelle nano-delivery system ($SUN_{b\text{-}PM}$), working in a synergistic manner with vaccine therapy in an advanced mouse melanoma model. $SUN_{b\text{-}PM}$ not only increased cytotoxic T-cell infiltration and decreased the number and percentage of MDSCs and Tregs in the TME, but also induced a shift in cytokine expression from Th2 to Th1 type while remodeling the tumor-associated fibroblasts, collagen, and blood vessels in the tumor. Additionally, inhibition of the Stat3 and AKT signaling pathways by $SUN_{b\text{-}PM}$ may induce tumor cell apoptosis or decrease tumor immune evasion. Our findings indicated that targeted delivery of a tyrosine kinase inhibitor to tumors can be used in a novel

*Corresponding author: leafh@unc.edu. (L. Huang).

synergistic way to enhance the therapeutic efficacy of existing immune-based therapies for advanced melanoma.

Graphical abstract

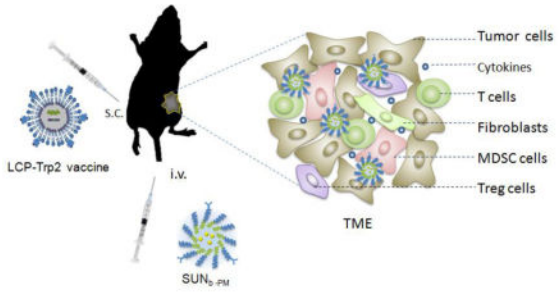

Keywords

Polymeric micelles; Sunitinib base; Peptide vaccine; Tumor microenvironment; Advanced Melanoma

1. Introduction

Immunotherapy holds much promise for the treatment of cancer [1–3]. A wide variety of approaches have been implemented in order to stimulate a range of innate and adaptive immune activities [4]. Strategies include the use of immunomodulatory antibodies, vaccines, and adoptive cell transfer [5–7]; however, most immunotherapeutic approaches on their own fall short of initial expectation when used against advanced malignancy [8]. Reasons for this limited success might be the immune-suppressive tumor microenvironment (TME) that presents in later tumor grades [9, 10]. Tumors are not just a mass of proliferating genetically abnormal cells; they are now well defined as a heterogeneous and structurally complex tissue. Malignant tumor cells can recruit a variety of cell types, including fibroblasts, immune inflammatory cells, and endothelial cells, through production and secretion of stimulatory growth factors and cytokines [11, 12]. This assortment of cells and molecules together comprises the TME. Antitumor immunity within the TME can be suppressed not only by tumor infiltrating leukocytes but also by tumor cells themselves through a number of mechanisms such as secretion of cytokines, expression of inhibitory receptors, or blockage of T cell function [13]. Many of these regulatory mechanisms can occur concurrently within the TME, resulting in multiple redundant levels of immune suppression, which reduces the effectiveness of immunotherapy. Therefore, development of an effective treatment against advanced tumors remains a major challenge for cancer immunotherapy.

The TME can impede immunotherapy, and approaches to specifically reduce immune suppression within the TME might be effective means to solve this problem. Sunitinib malate, an oral multi-target receptor tyrosine kinase inhibitor (TKI), has been approved by the Food and Drug Administration as a first line therapy for patients with metastatic renal cell cancer and proto-oncogene c-kit^{+} gastrointestinal stromal tumors [14]. Sunitinib has been shown to have a direct inhibitory effect on tumor growth by promoting tumor apoptosis

and inhibiting the tumor-promoting effect of vascular endothelial growth factor (VEGF) [15, 16]. In addition, sunitinib can indirectly inhibit tumor growth by stimulating anti-tumor immune responses [17–19]. Based on its well documented tumor apoptosis and immune adjuvant properties, as well as the over-expressed sigma receptors on the surface of melanoma cells, we hypothesize that targeted delivery of hydrophobic sunitinib base to the tumor using anisamide-modified poly-lactic-glycolic-acid-poly (ethylene glycol) (PLGA-PEG-MBA) polymeric micelles (PM) will result in a modulation of the TME and enhance the activity of vaccination against advanced tumors.

In our previous studies, we have successfully developed a potent mannose-modified lipid calcium phosphate (LCP) nanoparticle (NP)-based vaccine containing both tumor-specific antigen (tyrosinase-related protein 2 (Trp2) peptide) and adjuvant (CpG) to activate a mouse's dendritic cells [20, 21]. Results showed that the LCP-Trp2 vaccination could generate a strong *in vivo* cytotoxic T lymphocyte (CTL) response, which resulted in a potent anti-tumor immune response against the Trp2-expressing melanoma. Previous studies have also indicated that immunotherapy effectively inhibits tumor progression in a B16F10 melanoma model in the early stages of tumor progression (4 days after tumor inoculation). Unfortunately, vaccination with LCP-Trp2 at a later stage of tumor growth (13 days after tumor inoculation) is not very effective in inhibiting tumor growth, despite the fact that the systemic CTL response was the same [20]. Most likely, the immunotherapeutic efficiency was compromised because of increased immune suppression in the TME and faster tumor growth. Therefore, in the present study, a novel combined treatment was developed using intravenous delivery of sunitinib base in PLGA-PEG-MBA ($SUN_{b\text{-}PM}$) and subcutaneous delivery of the LCP-Trp2 vaccine to treat the advanced melanoma. We expected that the tumor-targeted sunitinib base could specifically modulate the TME and reverse its immune suppression, increasing the anti-tumor immune response of the vaccine and inhibiting growth of the late-stage tumor (Scheme 1).

2. Materials & Methods

2.1. Materials

Sunitinib base was purchased from Selleckchem (Houston, TX, USA). Sunitinib malate was purchased from Sigma-Aldrich (St. Louis, MO, USA). [^{3}H]sunitinib TFA salt was purchased from ViTrax (20 Ci/mmol) (Placentia, CA, USA). Acid-terminated PLGA (lactide/glycolide (50:50)) was purchased from DURECT (Pelham, AL, USA). mPEG3500-NH_2·HCl and tBOC-PEG3500-NH_2·HCl were ordered from JenKem Technology USA, Inc. (Allen, TX). MBA was purchased from Sigma-Aldrich (St. Louis, MO, USA). PLGA-PEG and PLGA-PEG-MBA were synthesized according to our previous publications and the structures were confirmed using ^{1}H NMR [22].1,2-Dioleoyl-3-trimethylammonium-propane chloride salt (DOTAP), 1,2-distearoryl-sn-glycero-3-phosphoethanolamine-N-[methoxy(polyethyleneglycol-2000)] ammonium salt (DSPE-PEG) and dioleoylphosphatydic acid (DOPA) were purchased from Avanti Polar Lipids (Alabaster, AL, USA). Cholesterol was purchased from Sigma-Aldrich (St. Louis, MO, USA). DSPE-PEG-Mannose was synthesized in our laboratory using DEPE-PEG-NHS (NOF, Shibuya-ku, Tokyo) and 4-Amino phenyl α-D-mannopyranoside (Sigma-Aldrich, St. Louis, MO) as

previously reported and the structure was confirmed using ^{1}H NMR[21]. H-2K^{b}-restricted peptides Trp2 (SVYDFFVWL, MW1175), OVA (SIINFEKL, MW1773) and modified Trp2 peptide, p-Trp2 (pSpSSSVYDFFVWL, MW1626) were purchased from Peptide 2.0 (Chantilly, VA, USA). CpG ODN 1826 (5′-TCCATGACGTTCCTGACGTT-3′) was obtained from Sigma-Aldrich (St. Louis, MO, USA). All other chemicals were purchased from Sigma-Aldrich (St. Louis, MO, USA).

2.2. Animals and tumor cell lines

Female C57BL/6 mice aged 6 to 8 weeks were purchased from the National Cancer Institute (Bethesda, MD). All animal procedures were carried out under protocols approved by the Institutional Animal Care and Use Committees at the University of North Carolina at Chapel Hill. Murine B16F10 melanoma cell lines syngeneic with C57BL/6 mice were obtained from American Type Culture Collection (ATCC) and cultured with DMEM supplemented with 10% fetal bovine serum, 100 U/mL penicillin and 100 μg/mL streptomycin (Invitrogen, Carlsbad, CA) at 37 °C and 5% CO_2.

2.3. Preparation of LCP-Trp2 vaccine

The LCP-based vaccine was prepared by a water-in-oil micro-emulsion technique as previously described [21]. Briefly, 600 μL $CaCl_2$ (2.5M) containing the phosphorylated Trp2 peptide and CpG ODN was dispersed in a 20 mL Cyclohexane/Igepal CO-520 (71:29, v/v) solution to form a well-dispersed Ca phase. Concurrently, 600 μL Na_2HPO_4 (12.5 mM, pH9.0) and 200 μL DOPA (20 mM) were dispersed in another 20 mL oil phase to obtain the phosphate phase. After the above micro-emulsion phases were stirred separately for 15 min, they were mixed together and stirred for another 30 min. Forty mL of ethanol was then added to break the micro-emulsion, and the calcium phosphate cores were collected by centrifugation (10,000 *g*× 20 min) and washed with ethanol 3 times. The pellets were dissolved in chloroform and mixed with 100 μL DOTAP (20 mM), 100 μL cholesterol (20 mM), 20 μL DSPE-PEG-2000 (20 mM), and 20 μL DSPE-PEG-mannose (20 mM). After evaporating the chloroform, the LCP vaccine particles were dispersed in 100 μL of 5% glucose. The morphologies of LCP NPs were observed by transmission electron microscopy (TEM) (JEOL 100CX II TEM, JEOL, Japan). Particle size and zeta potential were measured by a Malvern Zetasizer Nano ZS (Malvern, Worcestershire, UK).

2.4. Preparation and characterization of sunitinib base-loaded PLGA-PEG-MBA polymeric micelles ($SUN_{b\text{-}PM}$)

The solvent displacement method was employed to form the drug-loaded micelles [22]. Briefly, 0.7 mg of sunitinib malate or its free base and four mg of polymers (weight ratio of PLGA/PLGA-PEG/PLGA-PEG-MBA was fixed at 1:8:1) were dissolved in organic solvents (DMSO or THF). Micelles were formed by adding the drug-polymer solution dropwise into four mL of water under stirring at room temperature. The resulting suspension was allowed to stir uncovered for six h at room temperature to evaporate the organic solvent. The unencapsulated drug was removed by ultrafiltration (50,000 nominal molecular weight limit (NMWL), Millipore, Billerica, MA) at 4,000 *g* for 15 min. The drug-loaded micelles were then re-suspended, washed with water and stored in 5% glucose. The drug-loaded micelles were observed by TEM and particle size distributions/zeta potentials were determined using

a Malvern Zetasizer Nano ZS. Drug loading was measured using a UV spectrophotometer (Beckman Coulter, Atlanta, GA). Encapsulation efficiency (EE) and drug loading (DL) were calculated according to the formulas:

$$EE\,(\%) = \frac{mass\ of\ drug\ in\ PM}{mass\ of\ input\ drug\ used\ for\ PM\ preparation} \times 100\%$$
$$DL\,(\%) = \frac{mass\ of\ drug\ in\ PM}{total\ mass\ of\ loaded\ PM} \times 100\%$$

Stability was evaluated by determining the particle size and drug content during storage at 4 °C

2.5. In vitro release of sunitinib base from $SUN_{b\text{-}PM}$

In vitro release rates of sunitinib base from $SUN_{b\text{-}PM}$ in pH 7.4 or 5.8 were evaluated using a dialysis method. In order to establish a sink condition, 0.1% Tween-80 was added in the PBS. $SUN_{b\text{-}PM}$ with a final concentration of 300 μg/mL was placed into a dialysis tube with a molecular weight cut-off of 10,000 Da and dialyzed against 40 mL PBS in a thermo-controlled shaker with a stirring speed of 100 *rpm* at 37 °C. An aliquot (2 mL) was drawn at predetermined time intervals, and fresh release medium (2 mL, 37°C) was added. The content of original sunitinib base in the release medium was determined using Agilent 1260 HPLC equipped with a LIChrospherTM C18 column (particle size, 5 μm; 250 mm × 4.6 mm). The mobile phase and gradient elution method were shown in Table S1. The flow rate was 1.0 mL/min. The detection wavelength was 268 nm, sample injection volume was 20 μL, and the column temperature was 35 °C. The cumulative release amount at each time point was calculated from the percentage of the total solution that was taken in the aliquot (n = 6). Due to the degradation of the drug in release media (Figure S1), the release study was conducted only to 24 h to compare the release behavior of sunitinib base from micelles at different pH environments.

2.6. In vitro cytotoxicity studies

The *in vitro* cytotoxicity of sunitinib malate or $SUN_{b\text{-}PM}$ against the B16F10 cells was evaluated by the MTT assay. The free sunitinib malate solution was prepared by dissolving 12 mg of sunitinib malate in 1.0 mL DMSO. The samples containing the drugs were diluted with culture medium to obtain the desired sunitinib concentration, ranging from 1.25 to 60 μM. The B16F10 cell suspension in culture medium (DMEM+10% FBS) was seeded in 96-well plates at 4×10^3 cells/well and was incubated at 37 °C in a humidified atmosphere with 5 % CO_2 for 24 h. The cells were then treated with either $SUN_{b\text{-}PM}$ micelles or sunitinib malate solution. After incubation for 24 h, the MTT cell viability assay was performed as described previously [23].

2.7. Tumor targeting of $[^3H]SUN_{b\text{-}PM}$ in C57BL/6 mice bearing B16F10 tumors

Solid melanoma tumors were developed in C57BL/6 mice by subcutaneous inoculation of 2×10^5 B16F10 cells into the right flank of the mice. When the tumors grew to approximately 300 mm^3, tumor-bearing mice were treated *i.v.* with a single dose of 10 mg/kg $SUN_{b\text{-}PM}$ containing ^3H-labeled sunitinib base (TFA salt was neutralized by triethylamine) or treated *p.o.* with a single dose of 30 mg/kg SUN_{OS} containing ^3H-labeled sunitinib TFA salt. In

both the *i.v.* and *p.o.* groups, the dose of ^{3}H-labeled sunitinib was fixed at 50 μCi/kg. The mice were sacrificed six h, 12 h, and 24 h post-*i.v.* or *p.o.* administration. Tumor tissue samples were first digested by Tissue Solubilizer (Amersham Biosciences Corp. NJ, USA) overnight at room temperature and then added to four mL of scintillation cocktail (Thermo Fisher Scientific Inc., MA, USA). The samples were then assayed using a liquid scintillation counter (Beckman coulter LS6500). The percentage of the administrated dose (% ID) in the tissue was calculated and normalized to the total weight of each organ. All tests were done in triplicate.

2.8. Tumor growth inhibition

To assay whether $SUN_{b\text{-}PM}$ has improved therapeutic efficacy *in vivo* when used in combination with the Trp2 vaccine, a subcutaneous tumor was established by inoculating 2×10^5 B16F10 cells into the right flank of C57BL/6 mice. Sunitinib oral suspension (SUN_{OS}) was used as a control. SUN_{OS} was prepared according to a previous report, with slight modifications [24]. Briefly, sunitinib malate was directly suspended in a carboxymethylcellulose (CMC) solution (CMC 0.5 %, NaCl 1.8 %, and Tween 80 0.4 % in distillated water) with grinding. The final drug concentration in suspension was 3 mg/mL. When tumors grew to approximately 200 mm^3 (day 13), mice were randomly divided into six groups receiving different treatments as follows: (i) normal PBS (the control group, n=6); (ii) LCP-Trp2 vaccine at 200 μg Trp2/kg (n=6); (iii) SUN_{OS} at 30 mg/kg sunitinib malate (n=6); (iv) LCP-Trp2 vaccine at 200 μg Trp2/kg plus SUN_{OS} at 30 mg sunitinib malate/kg (n=6); (v) $SUN_{b\text{-}PM}$ at 10 mg sunitinib base/kg (n=6); (vi) LCP-Trp2 vaccine at 200 μg Trp2/kg plus $SUN_{b\text{-}PM}$ at 10 mg sunitinib base/kg. For the vaccine only and combination therapy groups, the vaccine was *s.c.* injected into the left flank of mice on day 14. Sunitinib was administered *p.o.* or *i.v.* every other day for three total administrations starting on day 14. The tumor volumes were measured every day and calculated as $A\times B^2/2$, where A was the largest diameter and B was the smallest. After completion of the therapeutic experiment on day 19, mice were humanely sacrificed and tumor tissue and major organs were collected for further experiments. The tumors were weighed and the inhibition ratio (IR) was defined as $IR\ (\%) = [(W_c - W_t)/W_c]\times 100$, where W_c and W_t are the average tumor weights for the control group and each treatment group, respectively.

To further evaluate the antitumor effect of $V+SUN_{b\text{-}PM}$ formulations on the animals, the tumors were fixed with 4 % (v/v) paraformaldehyde in PBS (pH 7.4) and sectioned into 5 μm slices. Apoptotic and non-apoptotic cells in tumor tissues were histologically evaluated with hematoxylin and eosin (H&E) staining and with the terminal deoxynucleotidyltransferase-mediated nick end labeling (TUNEL) assay, using a commercial apoptosis detection kit (Promega, Madison, WI). TUNEL-positive (apoptotic) cells had pyknotic nuclei with dark green fluorescent staining. Images of the sections were taken by a fluorescence microscope (Nikon, Tokyo, Japan). The apoptotic index was calculated by dividing the number of TUNEL-positive cells by the total number of cells in the field. Three randomly selected microscopic fields were quantitatively analyzed on ImageJ software.

2.9. Safety evaluation

To monitor the potential toxicity of the above regimens, we monitored animal behavior and relative weight loss throughout the *in vivo* therapeutic experiment. After the tumor growth inhibition study (section 2.8), blood samples and major organs were collected. Several biological markers for liver/kidney function were measured from the blood samples: alanine transaminase (ALT), aspartate transaminase (AST), alkaline phosphatase (ALP), blood urea nitrogen (BUN) and serum creatinine (Scr). The organs were fixed with 4% (v/v) paraformaldehyde in PBS (pH 7.4), embedded in paraffin, and sectioned into 5 μm slices. Each section was processed for H&E staining and examined by a board certified veterinary pathologist.

2.10. Flow cytometric evaluation of single-cell suspensions

Tumor-infiltrating and splenic lymphocytes were analyzed by flow cytometry. In brief, tumor and spleen tissues were harvested and digested with collagenase A and hyaluronidase at 37 °C for 40 min. After lysis of the red blood cells (RBCs), the dissociated cells were dispersed with 1 mL of HBSS. For intracellular cytokine staining, the cells from the tumor and spleen tissue were permeabilized with 0.1% triton X-100 for 15 min. The density of total cells was 5×10^6/mL. The tumor infiltrating immune cells were stained with the following fluorescence-labeled antibodies: FITC-conjugated anti-mouse CD8a, FITC-conjugated anti-mouse CD4, PE-conjugated anti-mouse Foxp3, FITC-conjugated anti-mouse CD11b, and PE-conjugated anti-mouse Gr-1 (BD, New South Wales, Australia). Flow cytometry was performed in quintuplicate for each group. Analysis was performed on a FACSCalibur flow cytometer and analyzed using Cell Quest software (BD Biosciences, San Jose, CA).

2.11. Immunofluorescence

Tissue section slides were processed *via* deparaffinization, antigen retrieval, permeabilization, and blocking with 1% bovine serum albumin (BSA) at room temperature for 1 h. MDSCs were defined using FITC-conjugated rat-anti-mouse CD11b and PE-conjugated rat-anti-mouse Gr1 (BD, New South Wales, Australia). Tregs were defined using FITC-conjugated rat-anti-mouse CD4 and PE-conjugated rat-anti-mouse Foxp3 (BD, New South Wales, Australia). T cells were defined using FITC-conjugated rat-anti-mouse CD8a (BD, New South Wales, Australia). Vessels and tumor-associated fibroblasts (TAF) were characterized by rabbit-anti-mouse CD31 and rabbit-anti-mouse α-SMA, and then treated with Alexa Fluor647-conjugated goat-anti-rabbit antibody. Nuclei were counterstained with DAPI (Vector Laboratories Inc, Burlingame, CA). All commercial binding reagents were diluted according to the manufacturer's recommendation. Images were taken using fluorescence microscopy (Nikon, Tokyo, Japan). Three randomly selected microscopic fields were quantitatively analyzed on ImageJ software.

2.12. Quantitative real-time PCR assay

Total RNA was extracted from tissue samples using an RNeasy kit (Qiagen, Valencia, CA) and cDNA was reverse-transcribed by a SuperScript First-Strand Synthesis System for RT-PCR (Invitrogen, Grand Island, NY). Amplification was conducted using the SSO Advanced

Universal Probe Supermix (Bio-rad, Hercules, CA), mouse-specific primers, and 100 ng of cDNA. Primers for mouse TGF-β, IL6, TNF-α, CCL2, IFN-γ, IL10, IL12a and IL2 were purchased from Life Technologies (Grand Island, NY). Mouse GAPDH primers were used as an endogenous control. The RT-PCR was performed in quintuplicate for each group. The reactions were conducted using a 7500 Real-Time PCR System, and the data were analyzed with the 7500 Software.

2.13. Masson trichrome staining

The Masson Trichrome assay was carried out to detect collagen in tumor tissues. Paraffin-embedded tumor sections were deparaffinized and rehydrated. The slides were then stained using a Masson Trichrome kit (Saint Louis, MO, USA) according to the manufacturer's instructions. Images were taken using light microscopy (Nikon, Tokyo, Japan). Three randomly selected microscopic fields were quantitatively analyzed on ImageJ software.

2.14. Change of tumor permeability

After a treatment schedule consistent with the tumor growth inhibition study (section 2.8), mice were i.v. injected with PLGA-PEG-MBA that was labeled with the lipophilic dye 1,1′-dioctadecyl-3,3,3′,3′-tetramethylindocarbocyanine perchlorate (DiI) at a dose of 0.5 mg/kg and were sacrificed 24 h post administration. Tumor tissue was harvested and stained with a fluorescein-conjugated CD11b antibody (BD Biosciences, San Jose, CA). Images were taken using fluorescence microscopy (Nikon, Tokyo, Japan). Three randomly selected microscopic fields were quantitatively analyzed on ImageJ software.

2.15. Western blot analysis

Western blots were performed on lysates generated from single-cell suspensions from tumors after different treatments as previously described. Primary antibodies were directed against p-stat3, stat3, p-AKT, and AKT (all from Cell Signaling, Beverly, MA) and GAPDH (Santa Cruz biotechnology, Dallas, TX). After washed blots were incubated with horseradish peroxidase (HRP)-conjugated secondary antibodies (Abcam, Cambridge, MA), signals were detected using the Pierce ECL Western Blotting Substrate (Thermo, Rockford, IL). Western blot was performed in triplicate for each group and the optical density of each protein band was analyzed with ImageJ software.

2.16. In vivo CTL response

The *in vivo* CTL assay was performed according to a previously described protocol [20]. In brief, splenocytes from naïve C57BL/6 mice were collected and pulsed with 10 μM Trp2 or Ova control peptides in complete media at 37°C for one h. Both pulsed cell populations were then stained with 2 μM PKH-26 (Sigma-Aldrich, St. Louis, MO) following the manufacturer's protocol. The Trp2 peptide-pulsed and Ova peptide-pulsed cells were then labeled with 4 μM and 0.4 μM carboxyfluorescein succinimidyl ester (CFSE), respectively. Eighteen C57BL/6 mice were divided into six groups and treated according to the schedule in section 2.8. Equal amounts of $CFSE^{high}$ (Trp2-pulsed cells) and $CFSE^{low}$ (Ova-pulsed cells) were mixed and *i.v.* injected into the treated mice. 18 h later, splenocytes were collected from these treated mice and subjected to flow cytometric analysis. The number of

CFSE^{high} and CFSE^{low} cells was calculated and the *in vivo* Trp2-specific lysis percentage was enumerated according to a published equation [20], also shown below. The *in vivo* CTL was performed in triplicate for each group.

$$\%\ Specific\ Lysis = \frac{(Ova * x - Trp2)}{(Ova * x)} * 100\%$$
$$Where\ x = \frac{Trp2}{Ova}\ from\ naïve\ mice$$

2.17. Statistical Analysis

Statistical analysis was performed by a Student's *t* test when comparing two groups, and by one-way ANOVA when comparing multiple groups. All results were expressed as mean ± S.D. unless otherwise noted. $p<0.05$ was considered statistically significant.

3. Results and Discussions

3.1. Preparation and characterization of $SUN_{b\text{-}PM}$

Polymeric micelle-based drug delivery systems are a powerful approach to deliver water-insoluble therapeutics to the tumor. Sigma receptors are well-known membrane-bound proteins that show high affinity for neuroleptics and are overexpressed on many human tumors including melanoma [25]. Therefore, MBA, an analog of anisamide and an agonist of sigma receptors, was used as a targeting ligand to further enhance the delivery of drugs to tumors. In this study, we encapsulated sunitinib into targeted PLGA-PEG-MBA micelles so that high bioavailability could be achieved in the tumor after systemic administration.

The physical entrapment of sunitinib into PLGA-PEG-MBA micelles was achieved by a well-established solvent displacement method [22]. The active ingredient in the commercial product Sutent® is the malate salt of sunitinib, which has a solubility in pure water of around 1 mg/mL [26]. The malate salt is used to increase the hydrophilicity of the drug for clinical use, which makes it much more difficult to load into the hydrophobic core of micelles. Although we found no papers on the preparation of nanoformulations containing sunitinib, the patents US 20120195826 A1 and WO 2014043625 A1 reported sunitinib malate nano-preparations based on PLGA-PEG or PLA-PEG micelles. Their studies showed a rather low drug loading content of less than 1 %. We also determined the loading amount and efficiency of Sunitinib malate into PLGA-PEG-MBA micelles. Not surprisingly, a low loading amount and encapsulation efficiency was obtained (5.1 % and 30.5 %, respectively) (Table 1).

Sunitinib base is more amenable to micellar encapsulation because its solubility in water is only ~1 % of that of sunitinib malate (4–8 μg/mL). Therefore, in the present study, sunitinib base was chosen as the therapeutic agent with which to prepare the drug-loaded micelles. Both DMSO and THF can dissolve the polymer and the drug, but it was found that using THF resulted in much higher drug loading and encapsulation efficiency than DMSO (Table 1, drug loading 14.2 % vs. 2.1 %; encapsulation efficiency 94.3 % vs. 12.1 %). This may occur because sunitinib base exhibits extremely high solubility in DMSO (> 40 mg/mL), and the strong interaction between DMSO molecules and drug molecules hampers the drug from

partitioning into the micelles. In contrast, sunitinib base exhibits only a moderate solubility in THF (~5 mg/mL), which is enough to dissolve the drug while still allowing the drug to associate highly with the polymer.

The particle size of $SUN_{b\text{-}PM}$ as measured by dynamic light scattering technology was around 73 nm (Table 1), suggesting that polymeric micelles should be able to selectively and efficiently accumulate in the tumor by means of the tumor's enhanced vessel permeability and decreased lymphatic drainage, termed the EPR effect [27]. Moreover, the particle size of $SUN_{b\text{-}PM}$ was much larger than blank micelles (73 nm vs 30 nm), indicating that the drug was actually loaded into the hydrophobic core of the micelles. The zeta potential of the drug-loaded micelles was around + 4 mV, which is similar to the zeta potential of the blank micelles.

TEM was also used to visualize the size and morphology of $SUN_{b\text{-}PM}$. As shown in Fig. 1B, $SUN_{b\text{-}PM}$ exhibited a spherical morphology with smooth surfaces. The observed micellar size was approximately 40–70 nm, which was slightly smaller than the hydrodynamic diameter obtained from the DLS experiment.

Most polymer micelles have poor physical stability after drug loading. In general, the stability of polymer micellar systems decreases as drug loading increases. PLGA-PEG-MBA micelles were found to possess an extremely high drug loading capacity for sunitinib base, and therefore it was necessary to further investigate its *in vitro* stability. Fig. 1C shows that the drug-loaded PLGA-PEG-MBA micellar solution could be stored at 4 °C for at least 4 months without a significant change in particle size and drug content, indicating excellent stability *in vitro*.

The *in vitro* release behaviors of sunitinib base from $SUN_{b\text{-}PM}$ in two different buffer solutions (pH 7.4 and 5.8) were studied and are shown in Fig. 1D. Sunitinib base releases from micelles much more slowly at pH 7.4 than at pH 5.8, likely because of the re-protonation of the amino group of sunitinib base at lower pH, which increases its ability to partition into water. This pH-dependent releasing behavior is of particular importance because it aids in achieving tumor-targeted drug delivery with micelles. It is expected that most sunitinib base that is encapsulated in micelles will remain in the micelle cores for a considerable time period when the injected micelles stay in the plasma at normal physiological conditions (pH 7.4); however, a faster release will occur once the micellar particles reach the solid tumor site where the local pH is reported to be one pH unit lower than that of normal tissue. In addition, micellar particles that are internalized into cells by endocytosis will encounter further acceleration of release inside the endosome/lysosome due to an additional decrease in pH [28].

The cytotoxicity of $SUN_{b\text{-}PM}$ against B16F10 cells was determined using an MTT assay and compared with sunitinib malate (Fig. 1E). The IC_{50} of $SUN_{b\text{-}PM}$ and sunitinib malate was 5.14 and 7.78 μM, respectively. The slightly enhanced cytotoxicity of $SUN_{b\text{-}PM}$ could be attributed to the targeted binding of the particles to the sigma receptors over-expressed on the surface of the B16F10 cells.

3.2. Preparation and characterization of p-Trp2 LCP vaccine

The LCP-based vaccine was prepared following the protocol we developed by our group [21]. As shown in Fig. 1A, the final LCP NPs containing both p-Trp2 peptide and CpG ODN were about 30 nm in diameter, determined by TEM after negative staining, which was slightly smaller than the measurement of the hydrodynamic diameter (40 – 45 nm) obtained by dynamic light scattering. The zeta potential was about 15 mV. The obtained vaccine was stored at 4 °C till use.

3.3. In vivo tumor-targeted delivery of sunitinib

We have successfully prepared $SUN_{b\text{-}PM}$ with high drug loading and excellent stability. To test whether PLGA-PEG-MBA could specifically deliver sunitinib base into tumors, *in vivo* tumor uptake studies were performed using ^{3}H-labeled sunitinib ([^{3}H] sunitinib) preparations in tumor-bearing mice. B16F10-bearing mice were administered 50 μCi/kg ^{3}H-labeled $SUN_{b\text{-}PM}$ *i.v.* or SUN_{OS} *p.o.* As shown in Fig. 2A, $SUN_{b\text{-}PM}$ showed two- to four-fold higher drug accumulation in tumors at all measured time points compared to the oral suspension. It can be concluded that PLGA-PEG-MBA can selectively target sunitinib base to tumors.

3.4. In vivo anti-tumor efficacy

To remodel the immunosuppressive tumor microenvironment, sunitinib malate is usually formulated as a suspension and given *p.o.* at a relatively high dose (20–70 mg/kg) for 7–14 consecutive days [16, 29, 30]. Once we confirmed the excellent tumor-targeting ability of $SUN_{b\text{-}PM}$ in the above tumor accumulation study, we wondered whether a low dose of sunitinib base delivered using targeted PLGA-PEG-MBA micelles could boost the tumor-specific immune response elicited by the LCP-Trp2 vaccine, thereby increasing antitumor efficiency.

In this study, B16F10 cells were subcutaneously inoculated in C57BL/6 mice and anticancer treatments were performed on tumors measuring ~200 mm^3. Tumor growth inhibition was tested in six groups of mice receiving PBS, VAC, SUN_{OS} (30 mg/kg, *p.o.*), $SUN_{b\text{-}PM}$ (10 mg/kg, *i.v.*), V+SUN_{OS} (30 mg/kg, *p.o.*), or V+$SUN_{b\text{-}PM}$ (10 mg/kg, *i.v.*). The tumor growth curve (Fig. 2B) shows that tumors in mice receiving VAC monotherapy elicited only partial tumor growth inhibition compared to the control mice that received only PBS treatment. This might be attributed to the strong suppressive tumor microenvironment in tumors at this advanced stage (14 days post tumor inoculation). Interestingly, SUN_{OS} and $SUN_{b\text{-}PM}$ both elicited greater anti-tumor efficacy than VAC monotherapy, and even though SUN_{OS} was given at a threefold higher dose, $SUN_{b\text{-}PM}$ showed similar antitumor efficacy. Among all groups, maximum tumor growth inhibition was achieved from the combination of V +$SUN_{b\text{-}PM}$. This result demonstrated that $SUN_{b\text{-}PM}$ could boost the tumor-specific immune response elicited by the Trp2 LCP vaccine, causing superior anti-tumor efficacy that was significantly more effective than V+SUN_{OS}. The inhibition ratios of all formulations were calculated based on the tumor weight at the end of the experiment (Fig. 2C) and were consistent with the results from tumor volume measurements.

The remarkable effect of V+$SUN_{b\text{-}PM}$ on the suppression of tumor growth is well supported by the histological cross-sections of the excised tumors. H&E-stained sections of tumor tissue from the PBS control group showed typical pathological characteristics of this tumor, such as closely arranged tumor cells and rich blood vessels (Fig. 2D). In contrast, the treated groups showed bulk necrosis and acellular regions. Among the five therapeutic groups, tumor tissues from the animals receiving V+$SUN_{b\text{-}PM}$ showed the fewest tumor cells and the highest antitumor efficacy. The TUNEL apoptosis assay in Fig. 2E also shows that the highest cellular apoptosis was generated from the V+$SUN_{b\text{-}PM}$ group, indicating once again that the best therapeutic effect resulted from this combination.

3.5. Safety evaluations

Our study was the first to intravenously administer the multikinase inhibitor sunitinib, so it was essential to evaluate the potential *in vivo* toxicity. Histological analysis of organs through H&E staining shows no morphological difference in major organs after treatment (Fig. S1), and body weight analysis of mice showed no significant weight loss or gain from any treatment (Fig. 3A). Hepatic and renal function was further evaluated using the serum of mice after treatment. The levels of biochemical parameters AST, ALT, ALKP, BUN, and Creatinine are shown in Fig. 3B and C. Tumor free mice were used as an additional control. The data shows that for all treatment groups, all parameters were in the normal range except AST, which was elevated in all tumor-bearing mice, consistent with reports about melanoma-associated toxicity [31]. After treatment, the level of AST decreased, and even reached the normal range in the group given V+$SUN_{b\text{-}PM}$, showing that this combination therapy can also normalize the hepatic function of tumor-bearing mice.

3.6. The change of immune cell populations in the TME

We hypothesized that targeted $SUN_{b\text{-}PM}$ provided more effective tumor growth inhibition because its higher tumor accumulation was more effective at remodeling the immunosuppressive TME. To test this hypothesis, the tumors and spleens from 5 groups of mice were analyzed for their suppressive immune cell populations using immunofluorescence and flow cytometry.

In tumor-bearing hosts, myeloid-derived suppressor cells (MDSCs) and T regulator cells (Tregs) play important roles in immune suppression, and the reversal of their function is vitally important for the success of immune therapy [32]. As shown in Fig. 4B, C, E, and F, an increase in MDSCs and Treg cells in the tumor was observed after LCP-Trp2 vaccine monotherapy. The same phenomenon has also been observed for IL2-based immunotherapy [33]. To combat this unfavorable upregulation, we tested whether targeted delivery of $SUN_{b\text{-}PM}$ could decrease $CD11b^+/Gr1^+$ MDSC accumulation and $CD4^+/Foxp3^+$ Treg development in B16F10 tumor-bearing C57BL/6 mice, as the high number of MDSCs and Tregs in the TME might be the main reason for the undesirable anti-tumor efficacy of vaccine monotherapy in these advanced tumors. Treatment groups that received either a high-dose of SUN_{OS} or a low dose of $SUN_{b\text{-}PM}$ showed a significant drop in the presence of intratumoral MDSCs and Tregs, and when combined with vaccine treatment, the percentage of MDSCs and Tregs remained as low as those of sunitinib monotherapy, indicating the strong ability of sunitinib to reverse the tumor's immune suppression.

Antitumor cytotoxic T cells, which are T cells that generally bear CD8 molecular markers on their surface, are of paramount importance in immune defense against tumors [34]. We therefore additionally measured the $CD8^+$ T cell infiltration in the TME (Fig. 4A and D). The result revealed that although vaccine treatment alone resulted in a significant increase in $CD8^+$ T cells, the large amount of immunosuppressive cells such as MDSCs and Tregs that accumulated in the TME could impair these T-cell effector functions and thus lead to poor tumor growth inhibition. It is interesting to note that although SUN_{OS} alone exhibited no significant effect on the $CD8^+$ T cells in the TME, $SUN_{b\text{-}PM}$ dramatically increased $CD8^+$ T cell infiltration to levels comparable to that of the vaccine. Not surprisingly, the combination treatment of V+$SUN_{b\text{-}PM}$ yielded the highest frequencies of $CD8^+$ T cells in the TME, which was as high as 18.4±2.3% ($p<0.001$ v.s. PBS group; $p<0.05$ v.s. VAC group).

The mechanisms for sunitinib to increase intra-tumor CD8 T cells while reducing intra-tumor MDSCs and Tregs are likely complicated. According to the published papers and our own studies, the mechanisms for reversing immune suppressive TME might include the following: a) sunitinib inhibits tyrosine kinases (TK) of VEGF receptor (VEGFR), PDGFR-α and –β, Fms-like TK-3 (Flt-3) and kit, which in turn inhibit the differentiation of dendritic cells (DCs) [35]; b) sunitinib enhances the frequency of myeloid DCs (mDCs), which induce strong killer T-cell response [36]; c) the inhibition of STAT3 and c-Kit by sunitinib might prevent the accumulation of MDSCs or directly induce the apoptosis of MDSCs [19, 37, 38]. Sunitinib treatment, alone or combined with vaccine, did not significantly change the overall percentage of $CD11b^+Gr1^+$ MDSC, $CD4^+Foxp3^+$Treg, or $CD8^+$ T cells in the spleen of tumor-bearing mice (Fig. S3).

3.7. In vivo cytotoxic T lymphocyte assay

To further evaluate the effect of combination therapy on the activity of antigen-specific $CD8^+$ killer T cells, an assay for antigen-specific CTL response was performed. In previous studies, we confirmed that the CTL activity elicited by the vaccine was independent of tumor status (early or advanced stage) [20], but the efficacy of the CTL response was profoundly affected by the immune microenvironment in the tumor. In the present study (Fig. 5), mice immunized with LCP-Trp2 were able to generate a Trp2-specific CTL response similar to that in a previous report [20]. Mice treated with $SUN_{b\text{-}PM}$ or SUN_{OS} alone did not exhibit any noticeable Trp2-speific CTL response. In contrast, mice receiving combination therapies of V+$SUN_{b\text{-}PM}$ or V+SUN_{OS} efficiently eliminated ~62.9 % and 68.2 % of Trp2-pulsed target cells, respectively, suggesting that combination therapy elicited a potent Trp2-specifc *in vivo* CTL response compared to monotherapy. While Fig. 4 shows that V+$SUN_{b\text{-}PM}$ can reduce suppressor cells and enhance $CD8^+$ T cell infiltration in the tumor, the CTL functional assay suggests that $SUN_{b\text{-}PM}$ can indirectly boost $CD8^+$ T-cell killing efficiency by blocking the suppressor cell activity.

3.8. Cytokine expression profiles in the TME after treatment

To further understand the mechanisms underlying the reversion of immune suppression mediated by $SUN_{b\text{-}PM}$, we investigated the change in the cytokine expression profiles in the TME after treatment. Cytokines are important protein mediators of the immune response. The cytokine content of the microenvironment can influence the balance of

immunosuppressive and immunosupportive factors within tumors [39]. The pro le of cytokines expressed by T cells during an immune response can be broadly categorized into two polarized groups, T helper 1 (Th1) and T helper 2 (Th2), which activate cell-mediated or humoral immunity, respectively. A Th1 response is typified by the expression of IFNγ, IL2, and IL12a, while Th2 responses are typified by CCL2, IL6, IL10, TGFβ, and TNFα expression. Previous studies suggest that a Th1 response is more effective in eliciting anti-tumor immunity and that Th2 cytokines inhibit the development of anti-tumor immunity [40]. A gradual loss in Th1 and increase in Th2 cytokine profiles has been observed during progressive tumor growth [41].

The cytokine expression after treatment is shown in Fig. 6. Treatment with sunitinib alone or combined with VAC resulted in a polarization of the immune response toward the cellular immune pathway promoting Th1 cytokine expression and reducing Th2 cytokine expression. The shift from Th2 to Th1 provides regulatory signals required for the priming of MHC class I-restricted $CD8^+$ CTLs, and the activated CTLs serve predominantly as immune effectors that induce apoptotic tumor cell death. Although IL12a, a Th1-type cytokine, exhibits a contrary tendency, it does not change the overall trend of cytokine transformation. It is also noteworthy that the Trp2-specific vaccine significantly increased the expression of IL10 in the TME, while exhibiting no significant effect on other Th2-type cytokines. The high level of IL10 might be responsible for the poor therapeutic effect of VAC treatment alone; however, after combined treatment with SUN_{OS} or $SUN_{b\text{-}PM}$, the level of IL10 significantly decreased.

Sunitinib treatment inducing a shift from a type 2-cytokine response to a type 1 response in the tumor has been reported many times in the literature [19, 42, 43], but the precise mechanism is not clear. Finke's study suggested that the increased type-1 response after the therapy may be partly attributable to a reduction in the elevated number of Treg cells and is independent of either tumor shrinkage or objective clinical responses in renal cell carcinoma (RCC) patients [44]. The reduction in Tregs cells could be an indirect effect because sunitinib did not alter the expansion of either Treg cells or T-effector cells. The changes in Treg cells is likely related to the fact that sunitinib decreases the expression of MDSC cells [44, 45]. Our study also showed that $SUN_{b\text{-}PM}$ could decrease the number of Tregs and MDSCs in the advanced melanoma model. Agreeing with Finke, the improved type-1 cytokine response along with a reduction in the type-2 cytokines following sunitinib treatment may also be linked to the reduction of Treg cells. Moreover, we also found that sunitinib therapy not only changed the immune cell populations, but also altered the tumor structure such as tumor-associated fibroblasts, collagen, blood vessels as well as the permeability of the tumor (Section 3.9). The favorable remodeling of TME might work together to promote cytokine shift from Th2 to Th1 polarization. Further studies are needed to clarify the mechanism of action of sunitinib in the advanced melanoma.

3.9. Structural changes in the TME: vasculature, tumor associated fibroblasts (TAF), collagen fibers, and tumor permeability

The hypoxic tumor environment results in an abnormal blood vessel network that allows metastatic tumor cells to escape and strongly prevents infiltration of anti-cancer treatments

into the tumor mass [46]. Restoration of the abnormal tumor vessel phenotype to normalized vasculature can restore a proper immune response in the TME. We therefore examined the vessel content and distribution as well as the morphological changes in the tumor by measuring areas positive for the blood vessel marker CD31 using immunofluorescence staining. As shown in Fig. 7A, vessels stained with red fluorescence were abundant and randomly distributed in the untreated tumor. Moreover, the vessels in the untreated group were thin and elongated due to the high pressure in the TME (white arrows in Fig. 7A), which can greatly impede the infiltration of contents from vessels. VAC alone significantly reduced the vessel concentration, consistent with the previous report that immunotherapies can reduce tumor vasculature through release of IFNI and II in the TME [13]; however, the vessels were still crushed under the high pressure in the TME. SUN_{OS} and $SUN_{b\text{-}PM}$ monotherapy exhibited an even stronger antiangiogenic effect, inhibiting angiogenesis likely by blocking the phosphorylation of VEGFRs, PDGFRs, and other receptors on the cell membrane of tumor endothelial cells [29]. Interestingly, the remaining vessels in sunitinib-treated groups exhibited a round and open morphology (white arrowheads in Fig. 7A), an effect that was more pronounced in the $SUN_{b\text{-}PM}$ group. The normalization of the tumor vasculature in response to treatment, as well as the apoptotic decrease in cell and collagen density, can significantly decrease the interstitial pressure in the TME, which may enhance the infiltration of lymphocytes and/or nanoparticles into the tumor [47]. To confirm this increase in tumor permeability, we measured the accumulation of DiI fluorescence in tumors using Dil-labeled PLGA-PEG-MBA PMs (Fig. 7A, green). The PBS group exhibited poor tumor permeability and only weak fluorescence was observed, but combined treatment with $V+SUN_{b\text{-}PM}$ elicited the strongest and most widespread fluorescence, indicating that the combination therapy induced the highest permeability of the tumor. The enhanced permeability of the tumor tissue also likely favored the infiltration of lymphocytes into the tumors [48], in addition to possibly increasing the drug accumulation in the tumor upon subsequent dosing.

In the TME, TAFs aid the tumor in immune modulation by impeding antitumor T cell function [49]. Therefore, the effect of VAC and SUN on TAFs was also investigated by staining for α-smooth muscle actin (α-SMA), a marker for TAFs. The α-SMA staining showed that VAC alone partially attenuated the amount of α-SMA-positive cells, while $V+SUN_{b\text{-}PM}$ almost completely eliminated the fibroblast population in the tumor tissue (Fig. 7B), indicating that the combination not only affected tumor cells, but also depleted TAFs.

The over-expressed collagens in tumors not only create a microenvironment that supports tumor cell survival and enhances cell migration, but they also act as ligands for the inhibitory receptor LAIR-1, which inhibits the function of multiple types of immune cells [50]. Thus, we used Masson's Trichrome staining to study the collagen content and the morphology of the treated tumors (Fig. 7C). B16F10 melanoma does not develop an extensive stromal structure compared to other solid tumors [51, 52], so stroma revealed by the collagen staining showed thin and elongated fibrous structures in the PBS-treated tumor (blue staining indicated by yellow arrows in Fig. 7C). $V+SUN_{b\text{-}PM}$ again showed the greatest collagen inhibition compared to the other treatment groups. Taken together, these data indicate that $V+SUN_{b\text{-}PM}$ elicited a significant change in the structural tumor microenvironment.

3.10. Signaling pathway determinations

Because sunitinib is a known tyrosine kinase inhibitor, we examined several major downstream signaling molecules of tyrosine kinases, including AKT and Stat3. The results show that VAC monotherapy significantly increased the p-Stat3 protein levels compared to the PBS-treated group ($p<0.001$). However, when the tumor-bearing mice were treated with V+$SUN_{b\text{-}PM}$, a significant decrease in the p-Stat3 level in the tumors was observed (Fig. 8). Stat3 is constitutively activated in diverse cancer cell types, including melanoma. Frequent Stat3 activation in tumor cells is largely due to Stat3 being a point of convergence for numerous tyrosine kinases, including VEGFR, PDGFR, EGFR, and Src [37]. The inhibition of p-Stat3 in tumor cells can inhibit tumor growth by inducing tumor cell apoptosis [53], which we show in Fig. 1 and 3. Stat3 is also activated in many types of tumor-associated immune cells, including myeloid cells, promoting tumor immune evasion as well as tumor angiogenesis [54]. Ablating Stat3 in tumor myeloid cells can increase dendritic cell activation, tumor Treg reduction, and $CD8^+$ T-cell activation [55]. Moreover, it was recently documented that Stat3 was critically involved in tumor accumulation of MDSCs, which play an important role in suppressing antitumor immune responses [56]. This literature suggests that the decreased p-Stat3 expression induced by sunitinib might be responsible for the change in the TME. We also measured a decrease in p-AKT expression as a result of V +$SUN_{b\text{-}PM}$, which could also have a profound effect on tumor growth and progression [57].

4. Conclusions

In this report, we found that tumor-targeted delivery of a low dose of sunitinib base in PLGA-PEG-MBA micelles decreased the number and percentage of MDSCs and Tregs in the TME, increased cytotoxic T cell infiltration, and changed the cytokine profiles and stromal structure of the tumor, thereby abrogating tumor-associated immune suppression and working synergistically with our vaccine therapy in advanced B16F10 melanoma tumor-bearing mice. Our studies provide evidence in an *in vivo* animal model that targeted delivery of tyrosine kinase inhibitors to tumors can be used in a novel synergistic way to enhance the therapeutic efficacy of existing immune-based therapies for advanced tumors.

Supplementary Material

Refer to Web version on PubMed Central for supplementary material.

Acknowledgments

The work was supported by NIH grants CA149363, CA149387, CA151652 and DK100664.

Abbreviations

LCP	lipid calcium phosphate
NP	nanoparticles
Trp2	tyrosinase-related protein 2 (Trp2)
TME	tumor microenvironment

PM	polymeric micelle
PLGA-PEG-MBA	anisamide modified poly-lactic-glycolic-acid-poly(ethylene glycol) (PLGA-PEG-MBA)
$SUN_{b\text{-}PM}$	sunitinib base-loaded polymeric micelles
SUN_{os}	sunitinib malmate oral suspension
TKI	tyrosine kinase inhibitor
VEGF	vascular endothelial growth factor
CTL	cytotoxic T lymphocyte
DPTAP	1,2-Dioleoyl-3-trimethylammonium-propane chloride salt
DSPE-PEG	1,2-distearoryl-sn-glycero-3-phosphoethanolamine-N-[methoxy(polyethyleneglycol-2000)] ammonium salt
DOPA	dioleoylphosphatydic acid
TEM	transmission electron microscopy
CMC	carboxymethylcellulose
IR	inhibition ratio
H&E staining	hematoxylin and eosin staining
TUNEL	terminal deoxynucleotidyl transferase-mediated nick end labeling
ALT	alanine transaminase
AST	aspartate transaminase
ALP	alkaline phosphatase
BUN	blood urea nitrogen
Scr	serum creatinine
RBCs	red blood cells
BSA	bovine serum albumin
TAF	tumor associated fibroblast
DiI	1,1′-dioctadecyl-3,3,3′,3′-tetramethylindocarbocyanine perchlorate
HRP	horseradish peroxidase
MDSC	myeloid-derived suppressor cells

Treg	T regulator cells
Th1	T helper 1
Th2	T helper2

References

1. Jiang T, Zhou C. The past, present and future of immunotherapy against tumor. Translational lung cancer research. 2015; 4:253–264. [PubMed: 26207213]
2. Makkouk A, Weiner GJ. Cancer immunotherapy and breaking immune tolerance: new approaches to an old challenge. Cancer research. 2015; 75:5–10. [PubMed: 25524899]
3. Wen Y, Kolonich HR, Kruszewski KM, Giannoukakis N, Gawalt ES, Meng WS. Retaining antibodies in tumors with a self-assembling injectable system. Molecular pharmaceutics. 2013; 10:1035–1044. [PubMed: 23419203]
4. Rini B. Future approaches in immunotherapy. Seminars in oncology. 2014; 41(Suppl 5):S30–40. [PubMed: 25438998]
5. Wen Y, Collier JH. Supramolecular peptide vaccines: tuning adaptive immunity. Current opinion in immunology. 2015; 35:73–79. [PubMed: 26163376]
6. Robinette RA, Heim KP, Oli MW, Crowley PJ, McArthur WP, Brady LJ. Alterations in immunodominance of Streptococcus mutans AgI/II: lessons learned from immunomodulatory antibodies. Vaccine. 2014; 32:375–382. [PubMed: 24252705]
7. Chia WK, Teo M, Wang WW, Lee B, Ang SF, Tai WM, Chee CL, Ng J, Kan R, Lim WT, Tan SH, Ong WS, Cheung YB, Tan EH, Connolly JE, Gottschalk S, Toh HC. Adoptive T-cell transfer and chemotherapy in the first-line treatment of metastatic and/or locally recurrent nasopharyngeal carcinoma. Molecular therapy : the journal of the American Society of Gene Therapy. 2014; 22:132–139. [PubMed: 24297049]
8. Niezgoda A, Niezgoda P, Czajkowski R. Novel Approaches to Treatment of Advanced Melanoma: A Review on Targeted Therapy and Immunotherapy. BioMed research international. 2015; 2015:851387. [PubMed: 26171394]
9. Johansson A, Hamzah J, Ganss R. More than a scaffold: Stromal modulation of tumor immunity. Biochimica et biophysica acta. 2015
10. Becker JC, Andersen MH, Schrama D, Thor Straten P. Immune-suppressive properties of the tumor microenvironment. Cancer immunology, immunotherapy : CII. 2013; 62:1137–1148. [PubMed: 23666510]
11. Gajewski TF, Schreiber H, Fu YX. Innate and adaptive immune cells in the tumor microenvironment. Nature immunology. 2013; 14:1014–1022. [PubMed: 24048123]
12. Kerkar SP, Restifo NP. Cellular constituents of immune escape within the tumor microenvironment. Cancer research. 2012; 72:3125–3130. [PubMed: 22721837]
13. Devaud C, John LB, Westwood JA, Darcy PK, Kershaw MH. Immune modulation of the tumor microenvironment for enhancing cancer immunotherapy. Oncoimmunology. 2013; 2:e25961. [PubMed: 24083084]
14. Blumenthal GM, Cortazar P, Zhang JJ, Tang S, Sridhara R, Murgo A, Justice R, Pazdur R. FDA approval summary: sunitinib for the treatment of progressive well-differentiated locally advanced or metastatic pancreatic neuroendocrine tumors. The oncologist. 2012; 17:1108–1113. [PubMed: 22836448]
15. Chinchar E, Makey KL, Gibson J, Chen F, Cole SA, Megason GC, Vijayakumar S, Miele L, Gu JW. Sunitinib significantly suppresses the proliferation, migration, apoptosis resistance, tumor angiogenesis and growth of triple-negative breast cancers but increases breast cancer stem cells. Vascular cell. 2014; 6:12. [PubMed: 24914410]
16. Jaini R, Rayman P, Cohen PA, Finke JH, Tuohy VK. Combination of sunitinib with anti-tumor vaccination inhibits T cell priming and requires careful scheduling to achieve productive immunotherapy. International journal of cancer. Journal international du cancer. 2014; 134:1695–1705. [PubMed: 24105638]

17. Farsaci B, Higgins JP, Hodge JW. Consequence of dose scheduling of sunitinib on host immune response elements and vaccine combination therapy. International journal of cancer. Journal international du cancer. 2012; 130:1948–1959. [PubMed: 21633954]
18. Draghiciu O, Nijman HW, Hoogeboom BN, Meijerhof T, Daemen T. Sunitinib depletes myeloid-derived suppressor cells and synergizes with a cancer vaccine to enhance antigen-specific immune responses and tumor eradication. Oncoimmunology. 2015; 4:e989764. [PubMed: 25949902]
19. Ozao-Choy J, Ma G, Kao J, Wang GX, Meseck M, Sung M, Schwartz M, Divino CM, Pan PY, Chen SH. The novel role of tyrosine kinase inhibitor in the reversal of immune suppression and modulation of tumor microenvironment for immune-based cancer therapies. Cancer research. 2009; 69:2514–2522. [PubMed: 19276342]
20. Xu Z, Wang Y, Zhang L, Huang L. Nanoparticle-delivered transforming growth factor-beta siRNA enhances vaccination against advanced melanoma by modifying tumor microenvironment. ACS nano. 2014; 8:3636–3645. [PubMed: 24580381]
21. Xu Z, Ramishetti S, Tseng YC, Guo S, Wang Y, Huang L. Multifunctional nanoparticles co-delivering Trp2 peptide and CpG adjuvant induce potent cytotoxic T-lymphocyte response against melanoma and its lung metastasis. Journal of controlled release : official journal of the Controlled Release Society. 2013; 172:259–265. [PubMed: 24004885]
22. Guo S, Lin CM, Xu Z, Miao L, Wang Y, Huang L. Co-delivery of cisplatin and rapamycin for enhanced anticancer therapy through synergistic effects and microenvironment modulation. ACS nano. 2014; 8:4996–5009. [PubMed: 24720540]
23. Yin T, Wu Q, Wang L, Yin L, Zhou J, Huo M. Well-defined redox-sensitive polyethene glycol-paclitaxel prodrug conjugate for tumor-specific delivery of paclitaxel using octreotide for tumor targeting. Molecular pharmaceutics. 2015; 12:3020–3031. [PubMed: 26086430]
24. Castillo-Avila W, Piulats JM, Garcia Del Muro X, Vidal A, Condom E, Casanovas O, Mora J, Germa JR, Capella G, Villanueva A, Vinals F. Sunitinib inhibits tumor growth and synergizes with cisplatin in orthotopic models of cisplatin-sensitive and cisplatin-resistant human testicular germ cell tumors. Clinical cancer research : an official journal of the American Association for Cancer Research. 2009; 15:3384–3395. [PubMed: 19417025]
25. Waterhouse RN, Chapman J, Izard B, Donald A, Belbin K, O'Brien JC, Collier TL. Examination of four 123I-labeled piperidine-based sigma receptor ligands as potential melanoma imaging agents: initial studies in mouse tumor models. Nuclear medicine and biology. 1997; 24:587–593. [PubMed: 9316089]
26. Website: http://www.eurodiagnostico.com/media/pdf/Sunitinib%20Malate%20(Sutent).pdf.
27. Saha RN, Vasanthakumar S, Bende G, Snehalatha M. Nanoparticulate drug delivery systems for cancer chemotherapy. Molecular membrane biology. 2010; 27:215–231. [PubMed: 20939772]
28. Yin T, Wang L, Yin L, Zhou J, Huo M. Co-delivery of hydrophobic paclitaxel and hydrophilic AURKA specific siRNA by redox-sensitive micelles for effective treatment of breast cancer. Biomaterials. 2015; 61:10–25. [PubMed: 25996409]
29. Farsaci B, Donahue RN, Coplin MA, Grenga I, Lepone LM, Molinolo AA, Hodge JW. Immune consequences of decreasing tumor vasculature with antiangiogenic tyrosine kinase inhibitors in combination with therapeutic vaccines. Cancer immunology research. 2014; 2:1090–1102. [PubMed: 25092771]
30. Bose A, Taylor JL, Alber S, Watkins SC, Garcia JA, Rini BI, Ko JS, Cohen PA, Finke JH, Storkus WJ. Sunitinib facilitates the activation and recruitment of therapeutic anti-tumor immunity in concert with specific vaccination. International journal of cancer. Journal international du cancer. 2011; 129:2158–2170. [PubMed: 21170961]
31. Kaiserman I, Amer R, Pe'er J. Liver function tests in metastatic uveal melanoma. American journal of ophthalmology. 2004; 137:236–243. [PubMed: 14962411]
32. Lindau D, Gielen P, Kroesen M, Wesseling P, Adema GJ. The immunosuppressive tumour network: myeloid-derived suppressor cells, regulatory T cells and natural killer T cells. Immunology. 2013; 138:105–115. [PubMed: 23216602]
33. Takehara Y, Satoh T, Nishizawa A, Saeki K, Nakamura M, Masuzawa M, Kaneda Y, Katayama I, Yokozeki H. Anti-tumor effects of inactivated Sendai virus particles with an IL-2 gene on angiosarcoma. Clinical immunology. 2013; 149:1–10. [PubMed: 23886549]

34. Bendle GM, Holler A, Downs AM, Xue SA, Stauss HJ. Broadly expressed tumour-associated proteins as targets for cytotoxic T lymphocyte-based cancer immunotherapy. Expert opinion on biological therapy. 2005; 5:1183–1192. [PubMed: 16120049]
35. Nishioka Y, Aono Y, Sone S. Role of tyrosine kinase inhibitors in tumor immunology. Immunotherapy. 2010; 3:107–116.
36. van Cruijsen H, van der Veldt AA, Vroling L, Oosterhoff D, Broxterman HJ, Scheper RJ, Giaccone G, Haanen JB, van den Eertwegh AJ, Boven E, Hoekman K, de Gruijl TD. Sunitinib-induced myeloid lineage redistribution in renal cell cancer patients: CD1c+ dendritic cell frequency predicts progression-free survival. Clinical cancer research : an official journal of the American Association for Cancer Research. 2008; 14:5884–5892. [PubMed: 18794101]
37. Xin H, Zhang C, Herrmann A, Du Y, Figlin R, Yu H. Sunitinib inhibition of Stat3 induces renal cell carcinoma tumor cell apoptosis and reduces immunosuppressive cells. Cancer research. 2009; 69:2506–2513. [PubMed: 19244102]
38. Ko JS, Zea AH, Rini BI, Ireland JL, Elson P, Cohen P, Golshayan A, Rayman PA, Wood L, Garcia J, Dreicer R, Bukowski R, Finke JH. Sunitinib mediates reversal of myeloid-derived suppressor cell accumulation in renal cell carcinoma patients. Clinical cancer research : an official journal of the American Association for Cancer Research. 2009; 15:2148–2157. [PubMed: 19276286]
39. Shurin MR, Lu L, Kalinski P, Stewart-Akers AM, Lotze MT. Th1/Th2 balance in cancer, transplantation and pregnancy. Springer seminars in immunopathology. 1999; 21:339–359. [PubMed: 10666777]
40. Zhang Q, Liu XY, Zhang T, Zhang XF, Zhao L, Long F, Liu ZK, Wang EH. The dual-functional capability of cytokine-induced killer cells and application in tumor immunology. Human immunology. 2015; 76:385–391. [PubMed: 25305457]
41. Jones EA, Pringle JH, Angel CA, Rees RC. Th1/Th2 cytokine expression and its relationship with tumor growth in B cell non-Hodgkin's lymphoma (NHL). Leukemia & lymphoma. 2002; 43:1313–1321. [PubMed: 12153001]
42. Wongkajornsilp A, Wamanuttajinda V, Kasetsinsombat K, Duangsa-ard S, Sa-ngiamsuntorn K, Hongeng S, Maneechotesuwan K. Sunitinib indirectly enhanced anti-tumor cytotoxicity of cytokine-induced killer cells and CD3(+)CD56(+) subset through the co-culturing dendritic cells. PloS one. 2013; 8:e78980. [PubMed: 24232460]
43. Barik S, Bhuniya A, Banerjee S, Das A, Sarkar M, Paul T, Ghosh T, Ghosh S, Roy S, Pal S, Bose A, Baral R. Neem leaf glycoprotein is superior than cisplatin and sunitinib malate in restricting melanoma growth by normalization of tumor microenvironment. International immunopharmacology. 2013; 17:42–49. [PubMed: 23747315]
44. Finke JH, Rini B, Ireland J, Rayman P, Richmond A, Golshayan A, Wood L, Elson P, Garcia J, Dreicer R, Bukowski R. Sunitinib reverses type-1 immune suppression and decreases T-regulatory cells in renal cell carcinoma patients. Clinical cancer research : an official journal of the American Association for Cancer Research. 2008; 14:6674–6682. [PubMed: 18927310]
45. Ghiringhelli F, Puig PE, Roux S, Parcellier A, Schmitt E, Solary E, Kroemer G, Martin F, Chauffert B, Zitvogel L. Tumor cells convert immature myeloid dendritic cells into TGF-beta-secreting cells inducing CD4+CD25+ regulatory T cell proliferation. The Journal of experimental medicine. 2005; 202:919–929. [PubMed: 16186184]
46. Krock BL, Skuli N, Simon MC. Hypoxia-induced angiogenesis: good and evil. Genes & cancer. 2011; 2:1117–1133. [PubMed: 22866203]
47. Oelkrug C, Ramage JM. Enhancement of T cell recruitment and infiltration into tumours. Clinical and experimental immunology. 2014; 178:1–8.
48. Bellone M, Calcinotto A. Ways to enhance lymphocyte trafficking into tumors and fitness of tumor infiltrating lymphocytes. Frontiers in oncology. 2013; 3:231. [PubMed: 24062984]
49. Zhou L, Yang K, Andl T, Wickett RR, Zhang Y. Perspective of targeting cancer-associated fibroblasts in melanoma. Journal of Cancer. 2015; 6:717–726. [PubMed: 26185533]
50. Rygiel TP, Stolte EH, de Ruiter T, van de Weijer ML, Meyaard L. Tumor-expressed collagens can modulate immune cell function through the inhibitory collagen receptor LAIR-1. Molecular immunology. 2011; 49:402–406. [PubMed: 21955987]

51. Guo ST, Lin CM, Xu ZH, Miao L, Wang YH, Huang L. Co-delivery of Cisplatin and Rapamycin for Enhanced Anticancer Therapy through Synergistic Effects and Microenvironment Modulation. Acs Nano. 2014; 8:4996–5009. [PubMed: 24720540]

52. Zhang J, Miao L, Guo S, Zhang Y, Zhang L, Satterlee A, Kim WY, Huang L. Synergistic anti-tumor effects of combined gemcitabine and cisplatin nanoparticles in a stroma-rich bladder carcinoma model. Journal of controlled release : official journal of the Controlled Release Society. 2014; 182:90–96. [PubMed: 24637468]

53. Al Zaid Siddiquee K, Turkson J. STAT3 as a target for inducing apoptosis in solid and hematological tumors. Cell research. 2008; 18:254–267. [PubMed: 18227858]

54. Kida H, Ihara S, Kumanogoh A. Involvement of STAT3 in immune evasion during lung tumorigenesis. Oncoimmunology. 2013; 2:e22653. [PubMed: 23482587]

55. Rebe C, Vegran F, Berger H, Ghiringhelli F. STAT3 activation: A key factor in tumor immunoescape. Jak-Stat. 2013; 2:e23010. [PubMed: 24058791]

56. Yang F, Hu M, Lei Q, Xia Y, Zhu Y, Song X, Li Y, Jie H, Liu C, Xiong Y, Zuo Z, Zeng A, Li Y, Yu L, Shen G, Wang D, Xie Y, Ye T, Wei Y. Nifuroxazide induces apoptosis and impairs pulmonary metastasis in breast cancer model. Cell death & disease. 2015; 6:e1701. [PubMed: 25811798]

57. Noh KH, Kang TH, Kim JH, Pai SI, Lin KY, Hung CF, Wu TC, Kim TW. Activation of Akt as a mechanism for tumor immune evasion. Molecular therapy : the journal of the American Society of Gene Therapy. 2009; 17:439–447. [PubMed: 19107122]

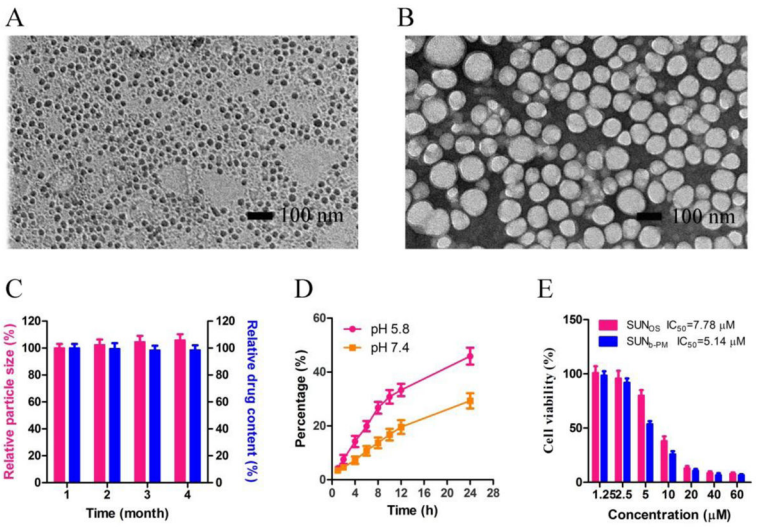

Fig. 1.

TEM images of (A) p-Trp2 LCP vaccine and (B) $SUN_{b\text{-}PM}$ after negative staining. (C) *In vitro* stability of $SUN_{b\text{-}PM}$ at 4°C. (D) *In vitro* release of sunitinib base from PLGA-PEG micelles at pH 5.8 and pH 7.4. (E) Cytotoxicity of SUN_{OS} and $SUN_{b\text{-}PM}$ against B16F10 cells after 24 h. The error bars in the graphs represent standard derivations (n=3).

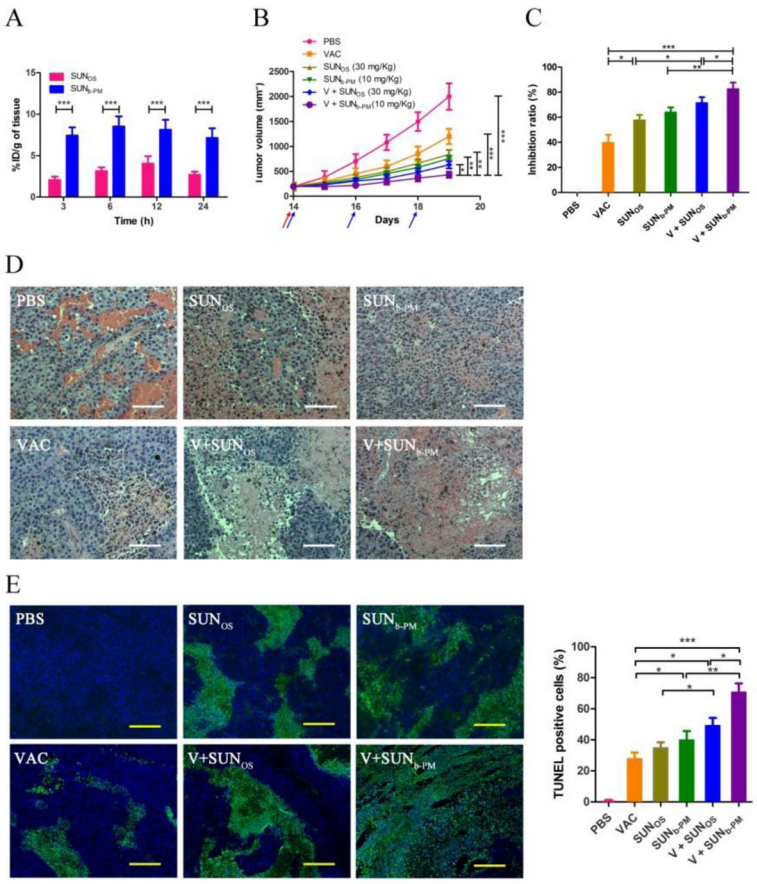

Fig. 2.

(A) Tumor accumulation of ^{3}H-labeled $SUN_{b\text{-}PM}$ and SUN_{OS} in C57BL/6 mice bearing B16F10 tumors at t = 3, 6, 12 and 24 h after treatment. The dose of ^{3}H-labeled drug was 50 μCi/kg. (B–E) Antitumor activity of PBS, VAC, SUN_{OS}, $SUN_{b\text{-}PM}$, V+SUN_{OS} and V +$SUN_{b\text{-}PM}$ on B16F10 tumor-bearing mice. C57BL/6 mice were inoculated with 2×10^{5} B16F10 cells on day 0. VAC was injected on day 14 at a dose of 0.3 mg/kg; SUN_{OS} was given *p.o.* or $SUN_{b\text{-}PM}$ was given *i.v.* on days 14, 16, and 18 at a dose of 30 mg/kg or 10 mg/kg, respectively. Tumor growth was measured every day until the 19th day after inoculation. Mice were sacrificed on day 19 and tumors were harvested. (B) Tumor volumes of tumor-bearing mice as a function of time. The arrows (pink for VAC and blue for SUN) indicate the time points of drug administration. (C) Tumor inhibition ratio calculated based on the weight of tumor at the end of the tests. (D) H&E staining of tumor sections. The white scale bar represents 100 μm. (E) TUNEL-positive cells in tumor sections excised from the mice seven days after the first treatment. The yellow scale bar represents 50 μm. Three randomly selected microscopic fields were quantitatively analyzed using ImageJ. The results are displayed as mean ± S.D. (error bars). Statistical analyses were calculated by comparing with the untreated group, unless otherwise specified. *$p < 0.05$, **$p < 0.01$, ***$p < 0.001$, $n = 5$.

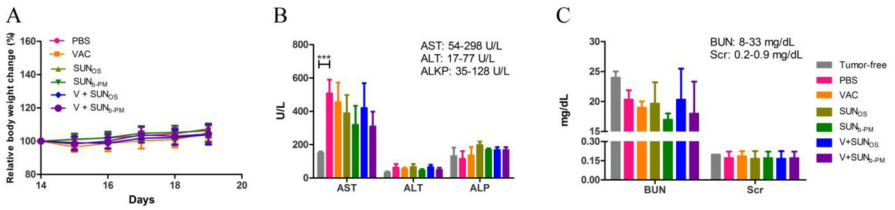

Fig. 3.

Safety evaluations. (A) Body weight change of B16F10-bearing mice after treatment with VAC, SUN_{OS}, $SUN_{b\text{-}PM}$, $V+SUN_{OS,}$ or $V+SUN_{b\text{-}PM}$. (B) Liver and (C) kidney function assays after treatment. Results were expressed as the mean ± S.D. (n = 5). The normal ranges for all the biochemical parameters are shown in the upper right corner of panels B and C.

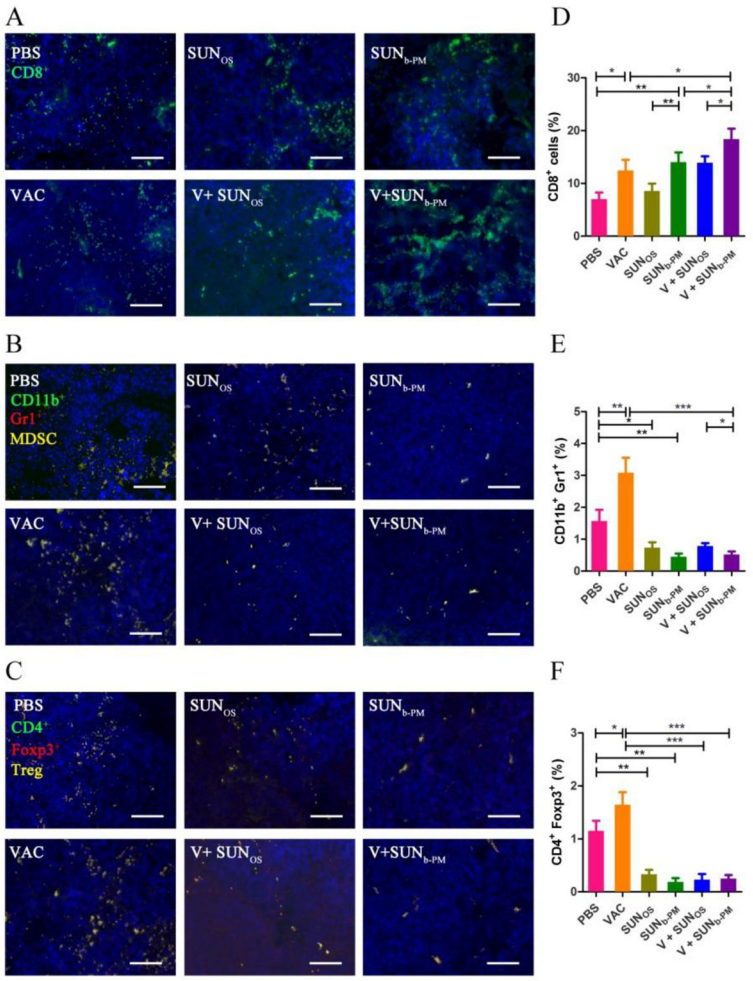

Fig. 4.

Tumor infiltrating immune cells after treatment. C57BL/6 mice were inoculated with 2×10^5 B16F10 cells on day 0. VAC was injected on day 14 at a dose of 0.3 mg/kg; SUN_{OS} and $SUN_{b\text{-}PM}$ were *p.o.* or *i.v.* administered on days 14, 16, and 18 at a dose of 30 mg/kg or 10 mg/kg, respectively. Mice were sacrificed on day 19 and tumors were harvested. Tumor tissues were assayed for $CD8^+$ T cells, $CD11b^+/Gr1^+$ MDSC cells, and $Foxp3^+/CD4^+$ Treg cells with immunofluorescence staining, and representative immunofluorescence images were presented (A-C). Flow cytometric analysis was also used to quantify immune cells in the TME (D-F). The results are displayed as mean ± S.D. (error bars). Statistical analyses were calculated by comparing to the untreated group unless otherwise specified with markings. *$p < 0.05$, **$p < 0.01$, ***$p < 0.001$, $n = 3$.

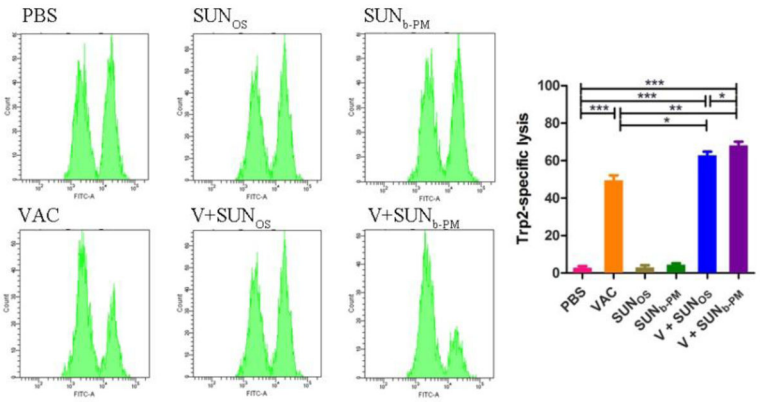

Fig. 5.

In vivo CTL response after vaccination under various conditions. C57BL/6 mice were subcutaneously injected with VAC on day 1, and treated with SUN_{OS} or $SUN_{b\text{-}PM}$ on days 1, 3 and 5. Splenocytes from naive mice were pulsed with Ova or Trp2 peptide and stained with low (Ova) or high (Trp2) concentrations of CFSE, respectively. The cells were then mixed and injected *i.v.* into the vaccinated mice. After 18 h, splenocytes from the vaccinated mice were analyzed by flow cytometry and enumerated according to a published equation [20]. A representative graph from each group is shown. $*p < 0.05$, $**p < 0.01$, $***p < 0.001$, $n = 3$.

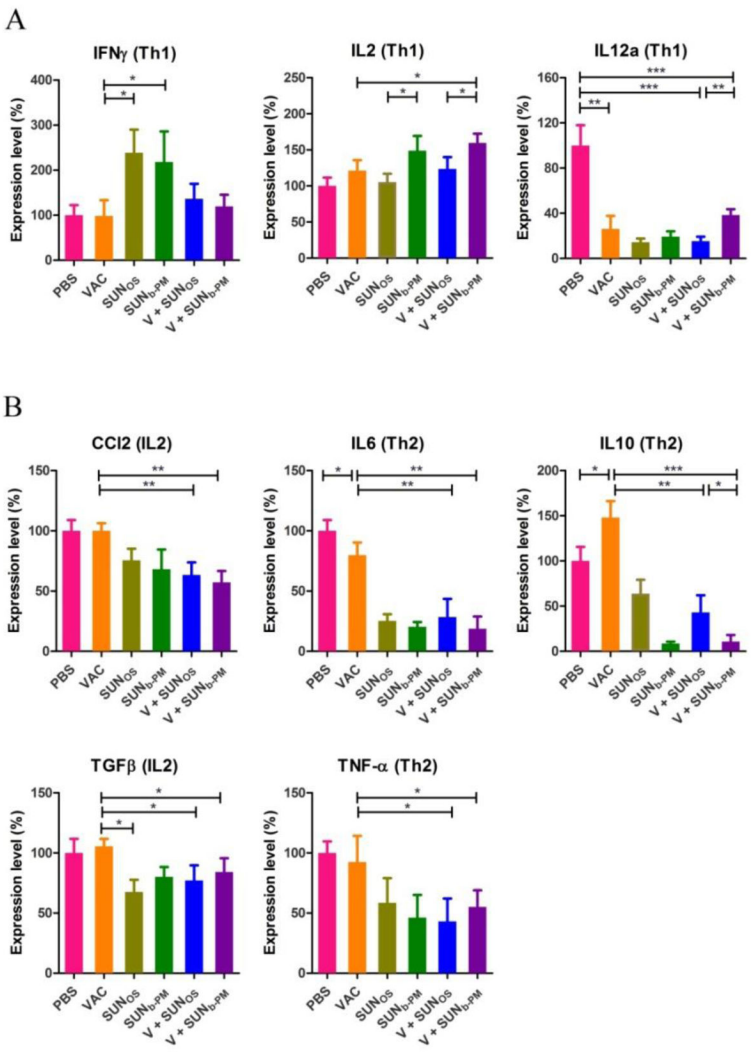

Fig. 6.

Tumor cytokine levels after vaccination. C57BL/6 mice were inoculated with 2×10^5 B16F10 cells on day 0. VAC was given on day 14 and SUN treatments were given on days 14, 16, and 18. Mice were sacrificed on day 18, and tumors were collected for cytokine detection using RT-PCR. The results are displayed as mean ± S.D. (error bars). Statistical analyses were calculated by comparison with the untreated group. *$p < 0.05$, **$p < 0.01$, ***$p < 0.001$, $n = 5$.

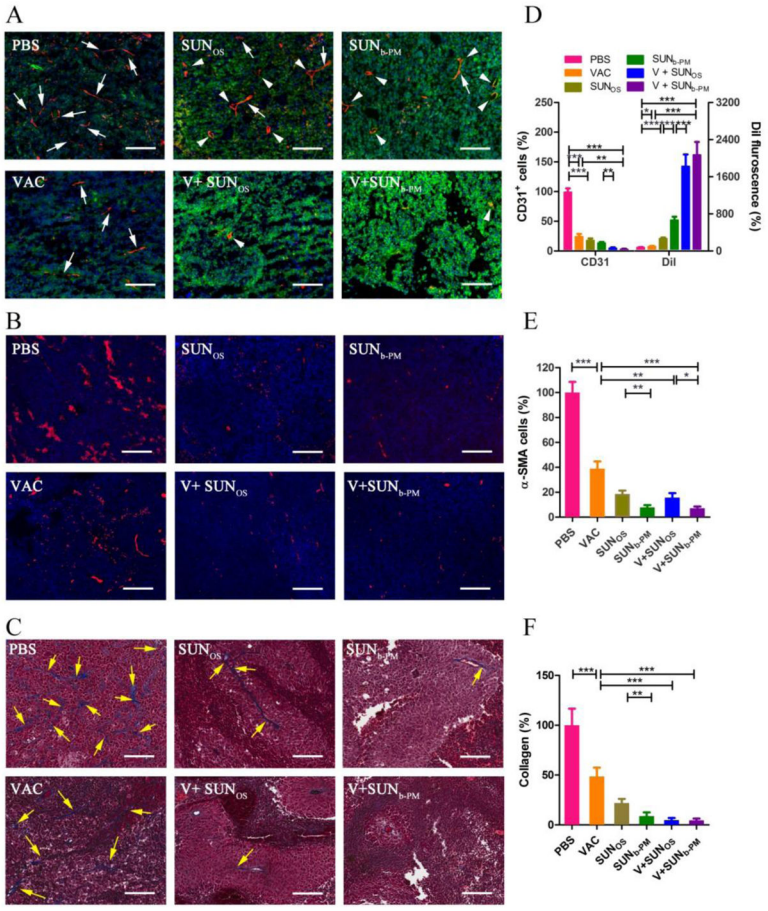

Fig. 7.

(A) Vessels in B16F10 tumors stained with CD31 antibody (red) to measure vasculature and DiI-labeled PLGA-PEG micelles (false color green) to measure tumor permeability. C57BL/6 mice were inoculated with 2×10^5 B16F10 cells on day 0. VAC was injected on day 14 at a dose of 0.3 mg/kg; SUN_{OS} and $SUN_{b\text{-}PM}$ were *p.o.* or *i.v.* administered on days 14, 16 and 18 at a dose of 30 mg/kg and 10 mg/kg, respectively. On day 19, the mice were *i.v.* injected with DiI-loaded PLGA-PEG micelles. Twenty four h after injection, the mice were sacrificed and tumors were harvested. The blood vessels were stained using an anti CD31 antibody; the cell nucleus was stained using DAPI (blue); the PLGA NPs were labeled with DiI. The white scale bar represents 100 μm. The white arrows indicate the thin and elongated vessels; the white arrowheads indicate the round and open vessels. (B) TAFs in tumors stained with α-SMA antibody (red), scale bar = 50 μm; (C) tumor sections stained with Masson's Trichrome, scale bar = 50 μm. The tumor-bearing mice in (B) and (C) were treated according to the above schedule and sacrificed on day 19. In (C), the blue color represents collagen fibers (yellow arrows). To quantify the fields, three randomly selected microscopic fields were quantitatively analyzed using ImageJ (D, E, F). The results are displayed as mean ± S.D. (error bars). Statistical analyses were calculated by comparing to the untreated group unless otherwise specified. $*p<0.05, **p<0.01, ***p<0.001, n=3.$

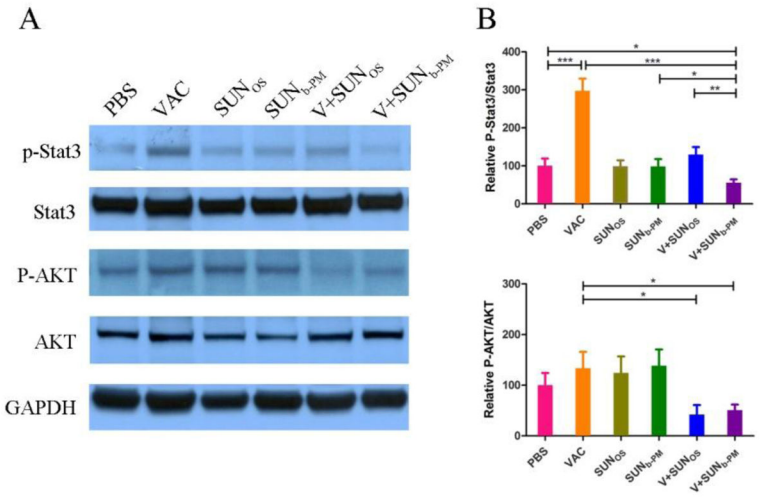

Fig. 8.

Expression levels of p-Stat3, Stat3, p-AKT, AKT, and GAPDH in tumor samples after treatment. C57BL/6 mice were inoculated with 2×10^5 B16F10 cells on day 0. VAC was injected on day 14 at a dose of 0.3 mg/kg; SUN_{OS} and $SUN_{b\text{-}PM}$ were administered *p.o.* or *i.v.* on days 14, 16, and 18 at a dose of 30 mg/kg and 10 mg/kg, respectively. Mice were sacrificed on day 19 and tumors were collected for western blot analysis. The results are displayed as mean ± S.D. (error bars). Statistical analyses were calculated by comparing with the untreated group unless specified with markings. *$p < 0.05$, **$p < 0.01$, ***$p < 0.001$, $n = 5$.

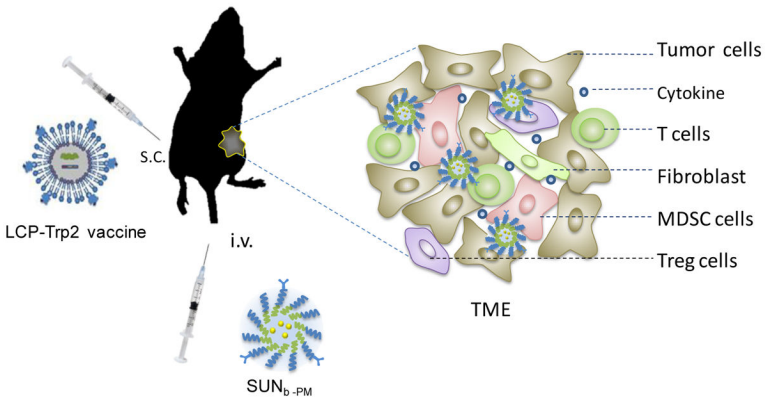

Scheme 1.

Schematic illustration of $SUN_{b\text{-}PM}$ and LCP-Trp2 vaccine injected into the advanced melanoma-bearing mouse.

Table 1

Loading of Sunitinib malate and sunitinib base into PLGA-PEG-MBA micelles

Drug	Organic solvent for drug/polymers	DL (%)	EE (%)	Particle size (nm)	PDI	Zeta potential (mV)
Sunitinib malate	DMSO	0.8±0.2	4.5±0.9	80.0±4.4	0.23±0.02	4.1±0.3
Sunitinib malate	THF	5.1±0.3	30.5±1.9	81.5±4.1	0.18±0.02	3.8±0.6
Sunitinib base	DMSO	2.1±0.1	12.1±0.9	78.3±3.9	0.19±0.02	4.2±0.6
Sunitinib base	THF	14.2±0.2	94.3±1.9	73.1±4.8	0.17±0.01	4.7±0.7